


# Characterization of Cell Membrane Permeability *In Vitro* Part I: Transport Behavior Induced by Single-Pulse Electric Fields\*

Technology in Cancer Research & Treatment  
Volume 17: 1-15  
© The Author(s) 2018  
Article reuse guidelines:  
sagepub.com/journals-permissions  
DOI: 10.1177/1533033818792491  
journals.sagepub.com/home/tct  


Daniel C. Sweeney, PhD<sup>1</sup> , James C. Weaver, PhD<sup>2</sup>,  
and Rafael V. Davalos, PhD<sup>1</sup>

## Abstract

Most experimental studies of electroporation focus on permeabilization of the outer cell membrane. Some experiments address delivery of ions and molecules into cells that should survive; others focus on efficient killing of the cells with minimal temperature rise. A basic method for quantifying electroporation effectiveness is measuring the membrane's diffusive permeability. More specifically, comparisons of membrane permeability between electroporation protocols often rely on relative fluorescence measurements, which are not able to be directly connected to theoretical calculations and complicate comparisons between studies. Here we present part I of a 2-part study: a research method for quantitatively determining the membrane diffusive permeability for individual cells using fluorescence microscopy. We determine diffusive permeabilities of cell membranes to propidium for electric field pulses with durations of 1 to 1000  $\mu$ s and strengths of 170 to 400 kV/m and show that diffusive permeabilities can reach  $1.3 \pm 0.4 \times 10^{-8}$  m/s. This leads to a correlation between increased membrane permeability and eventual propidium uptake. We also identify a subpopulation of cells that exhibit a delayed and significant propidium uptake for relatively small single pulses. Our results provide evidence that cells, especially those that uptake propidium more slowly, can achieve large permeabilities with a single electrical pulse that may be quantitatively measured using standard fluorescence microscopy equipment and techniques.

## Keywords

transport, propidium, pulsed electric fields, diffusion, electroporation

## Abbreviations

ATP, adenosine triphosphate; DMEM, Dulbecco's modified Eagle's medium; EP, electroporation; HEPES, 4-(2-hydroxyethyl)-1-piperazineethanesulfonic acid; PBS, phosphate-buffered saline; PEF, pulsed electric field; Pro, propidium; SFDF, serum-free DMEM/F12 medium

Received: February 9, 2018; Revised: June 18, 2018; Accepted: July 3, 2018.

## Introduction

Pulsed electric fields (PEFs) are effective in overcoming the transport barrier of the cell membrane by increasing its permeability. When a cell is exposed to a sufficiently strong PEF, nanoscale defects form in its membrane which allow low-molecular-weight solutes to more readily flow into and out of the cell.<sup>1,2</sup> Termed electroporation (EP), this process has been shown to affect cellular viability at even larger electric field strengths. A specific motivation for the basic studies reported

\*Part II of this paper is available online at <http://journals.sagepub.com/doi/full/10.1177/1533033818792490>.

<sup>1</sup> Department of Biomedical Engineering and Mechanics, Virginia Tech, Blacksburg, VA, USA

<sup>2</sup> Harvard-MIT Division of Health Sciences and Technology, Massachusetts Institute of Technology, Cambridge, MA, USA

## Corresponding Author:

Daniel C. Sweeney, PhD, Department of Biomedical Engineering and Mechanics, Virginia Tech, 329 Kelly Hall, 325 Stanger St, Blacksburg, VA 24061, USA.

Email: [sweeneyd@vt.edu](mailto:sweeneyd@vt.edu)



Creative Commons Non Commercial CC BY-NC: This article is distributed under the terms of the Creative Commons Attribution-NonCommercial 4.0 License (<http://www.creativecommons.org/licenses/by-nc/4.0/>) which permits non-commercial use, reproduction and distribution of the work without further permission provided the original work is attributed as specified on the SAGE and Open Access pages (<https://us.sagepub.com/en-us/nam/open-access-at-sage>).

here is irreversible EP, a nonthermal ablation technique that destabilizes a tissue's constituent cells to directly induce cell death.<sup>3-5</sup> To this end, nuclear condensation, DNA fragmentation, and altered metabolism are evident in cells following EP treatment,<sup>6,7</sup> and increased transmembrane ionic currents have also been observed electrically in electroporated cells.<sup>8</sup> However, there is currently not a robust experimental method to directly assess cellular permeability following EP treatments beyond relative comparisons. The absence of such a metric has impeded the direct validation of computational models with experimental cellular permeability data.

Following PEF application, a cell membrane can gradually reseal.<sup>9</sup> The greater the duration of the permeability increase, the less viable the local cell population will become.<sup>1,10</sup> This loss of viability is attributed to the formation of pores within the cell membrane driven by a large transmembrane potential.<sup>11,12</sup> Pores decrease the membrane's ability to inhibit the flow of solutes into and out of the cell.<sup>13,14</sup> The degree to which molecules flow through a membrane following PEF application is often due to the membrane's enhanced diffusive permeability. This quantity is widely used to study membrane dynamics following PEF application.<sup>15-18</sup> Small-molecule tracers, including propidium (Pro), have been developed to emit a strong fluorescence signal when metabolized or bound to intracellular structures but are blocked by an intact membrane. Through calibration, such molecules are used to measure molecular flow into cells following PEF application.<sup>19-22</sup> Measuring the diffusive permeability of a cell has also been proposed as a quantitative method of comparison between different PEF applications.<sup>23</sup> However, such measurements have not been reported beyond recent estimates involving PEFs with thousands of pulses.

In part I of our 2-part report, we quantify the increase in the diffusive permeability of cell membranes following single-pulse PEF application. In part II, we develop a computational model of cellular EP using the data provided herein in part I. Here, we show that the permeability of a cell membrane in the minutes following the application of an electrical pulse is a good indicator of the ultimate molecular uptake and that the cell remains permeable to Pro ions for tens of minutes following PEF application. This is, to our knowledge, the first report to provide a method to quantitatively measure membrane permeability to small molecules using standardized fluorescence microscopy techniques and equipment. We report the first of such measurements from individual cells following the application of a single electrical pulse within a microfluidic chamber. Our chamber was designed to allow the observation of cells exposed to different electric field strengths simultaneously. We also identify a subpopulation of cells that exhibit a prolonged uptake of Pro at lower strengths and shorter pulse durations than is generally required to elicit a larger, more rapid uptake response. Our results further indicate that it may be possible to effectively apply EP treatments with a single electrical pulse, resulting in less thermal damage than would be generated by longer pulse trains.

## Materials and Methods

### Microfluidic Chamber Design and Preparation

A microfluidic chamber was designed to allow cells within it to be exposed to varying electric field strengths and imaged simultaneously (Figure 1A and B). The geometry of the chamber was designed to an electric field with a magnitude that varies linearly along the length of the chamber (Figure 1C-F) by tapering the chamber along its length according to the equation  $y(x) = a/(x + b)$ , with appropriate boundary conditions ( $y(0) = 0.63$  mm and  $y(10$  mm) = 0.13 mm;  $a = 1.6$  and  $b = 2.5$ ).<sup>24</sup> The height of the chamber was 0.1 mm. To solve for the electric potential field within the chamber, Poisson equation ( $-\nabla \cdot (\sigma \nabla u) = 0$ , where  $u$  is the scalar electric potential field and  $\sigma$  is the buffer conductivity) was formulated as a boundary value problem with homogenous conductivity in the 3-dimensional, source-free chamber interior. A first-order tetrahedral mesh was generated using GMSH (version 2.9.3)<sup>25</sup> for analysis within the FEniCS finite element environment (version 2016.2.0).<sup>26</sup> Dirichlet boundary conditions were prescribed for the cylindrical regions at either end of the chamber that represent the electrode surfaces inserted into the chamber and set to the steady state voltage obtained from the 10-, 100-, and 1000-microsecond pulses (Supplemental Figure 1). No-flux Neumann boundary conditions were prescribed to all other chamber boundaries. The numerical error was calculated under the  $L^2$  norm and the mesh of the chamber iteratively refined until the relative error between 2 consecutive solution refinements were <5%. The electric field values reported were calculated from the voltage measured at the electrode after the ringing on the rising edge had stabilized (ie, 170, 250, 320, and 400 kV/m; Figure 2). The same naming convention was followed for the 1-microsecond pulse for consistency, recognizing that ringing dominates its waveform and is not accurately described by a single value. Using a scheme similar to the applied electric field, the heat equation was solved within the chamber using the electric field strength using FEniCS. The temperature distribution  $T$  was determined by solving  $\partial_t T - \alpha \nabla^2 T = \sigma \nabla u \cdot \nabla u$ , where  $\sigma$  is the conductivity of the extracellular buffer and  $\alpha = 0.14 \times 10^{-6}$  m<sup>2</sup>/s is the thermal diffusivity. Initially, the chamber temperature was uniformly set to 22°C. A backward finite difference scheme was implemented for temporal discretization, and the chamber domain was spatially discretized using the same mesh used to solve for the scalar electric potential field.

The physical chamber design was patterned on a silicon wafer using deep reactive ion etching and then placed under a vacuum for 1 hour. Polydimethylsiloxane (PDMS; Sylgard 184, Dow Corning, Midland, Michigan) was mixed in a ratio of 10:1 monomer to cross-linker, degassed under a vacuum, poured over the silanized negative master mold, and heated at 65°C. After 15 minutes, the temperature was increased to 100°C for at least an hour before the mold was allowed to cool to room temperature. Once cool, the cured PDMS block containing the master negative was removed from the mold. Holes

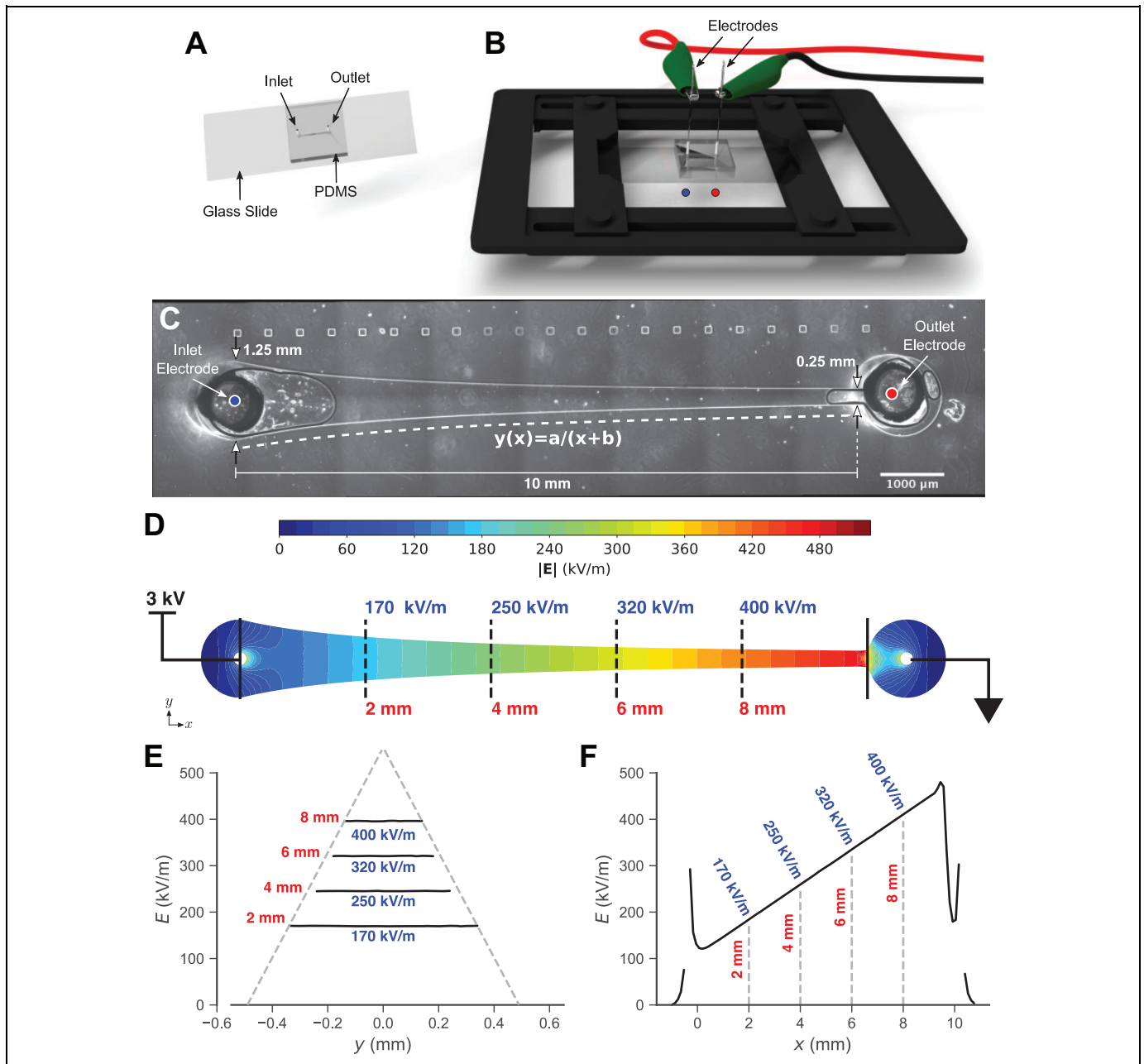


**Figure 1.** Microfluidic chamber for exposing cells to electric fields,  $E$ . **A**, The microdevice was comprised of a PDMS mold plasma bonded to a glass slide. **B**, The microfluidic chamber was placed on a microscope stage with needle electrodes inserted into the inlets on both sides of the chamber. **C**, The geometry of the microfluidic chamber is shown as well as the insertion locations for the stainless-steel electrodes (0.18 mm OD) marked in red and blue. The depth of the chamber is 0.1 mm. **D**, The electric field strength increases linearly along the axial direction ( $x$ -axis) of the tapered microfluidic chamber. Stainless steel electrodes are present at either end of the chamber to generate  $E$  during voltage application. **E**,  $E$  is presented as a function of distance along the vertical axis of the chamber  $y$  at 2, 4, 6, and 8 mm along the horizontal (dotted black lines in **B**). The dotted gray lines indicate the chamber boundaries. **F**,  $E$  is also presented as a function of the distance along the horizontal axis of the chamber. The dotted gray lines indicate the positions within the chamber at which the cells were observed. PDMS indicates polydimethylsiloxane.

were punched in both ends of the chamber (Figure 1A) using a 24 AWG biopsy punch (Integra LifeSciences, Plainsboro, New Jersey) to allow access to the chip interior once assembled. The surface of the cured PDMS containing the negative features of the silicon master was then plasma bonded to a 1-mm thick glass slide that served as the base of the chamber to complete

the fabrication process to enable imaging of the chamber contents (Figure 1B). For confocal imaging, a 0.1-mm thick glass slide was used. CHO-K1 cells (ATCC, Manassas, Virginia) were cultured in Ham F12-K medium (Gibco, Grand Island, New York) supplemented with 10% fetal bovine serum (FBS; Atlanta Biologicals, Flowery Branch, Georgia) and

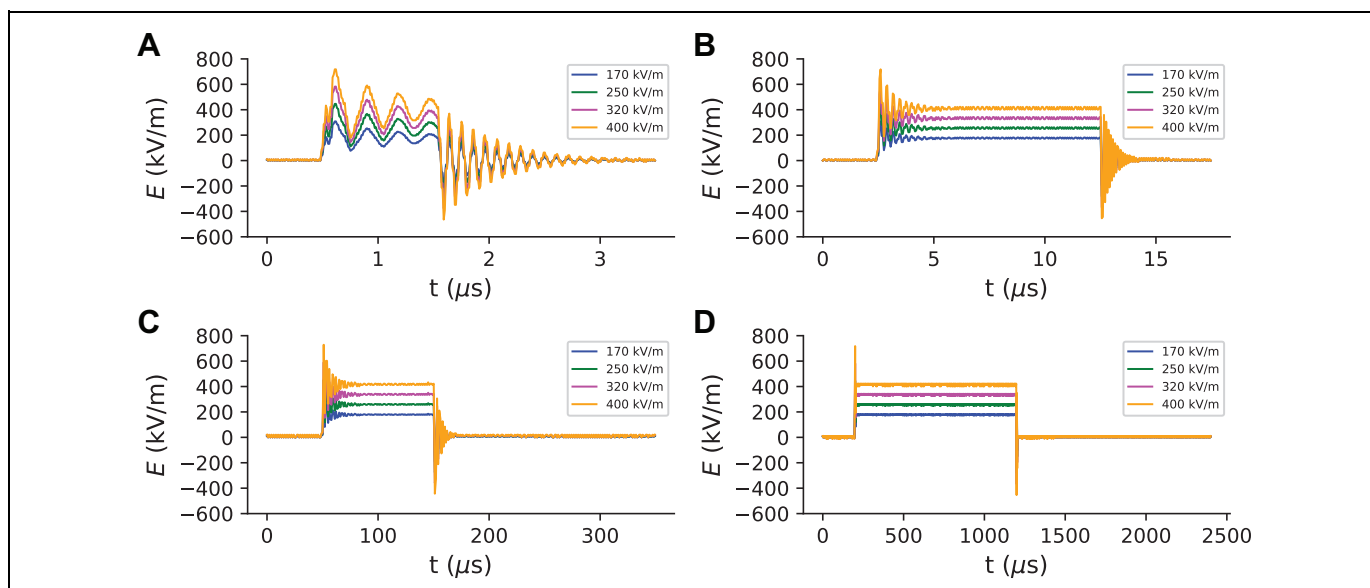


**Figure 2.** The  $E$  at each point in the chamber is estimated using voltage measurements at the 2 electrodes and the chamber geometry. Pulse durations include waveforms of A, 1  $\mu$ s, B, 10  $\mu$ s, C, 100  $\mu$ s, and D, 1000  $\mu$ s applied to a chamber containing PBS. In each figure,  $E$  is presented as a function of time  $t$ . Significant ringing exists on the rising and falling edges of each pulse and is consistently present between each pulse waveform.  $E$  is estimated using voltage traces (Supplemental Figure 1) as the Dirichlet boundary conditions on the electrode surfaces and solving for the static field inside the chamber. In these calculations, it is assumed that the medium in the chamber is purely ohmic. The labels 170, 250, 320, and 400 kV/m are derived from the  $E$  values at positions 2, 4, 6, and 8 mm along the long axis of the microfluidic chamber (Figure 1), simulated using an idealized square pulse in an ohmic environment. These values are indicated by the steady-state portions of the square wave in this representation. For simplicity, each value of  $E$  is referenced using these labels. Oscillations are of similar magnitude and duration for pulses applied to chambers containing each of the buffers. PBS indicates phosphate-buffered saline.

1% penicillin/streptomycin (penn/strep; Life Technologies, ThermoFisher Scientific, Waltham, Massachusetts). At 70% to 90% confluence, the cells were trypsinized; counted using a ViCell cell counter (Beckman-Coulter, Indianapolis, Indiana); resuspended in fresh medium containing 2 drops/mL of NucBlue (Life Technologies), 10% FBS, and 1% penn/strep with a concentration of cells  $1 \times 10^6$  cells/mL; and injected into the microfluidic chamber using 24 AWG PTFE tubing (Cole-Parmer, Vernon Hills, Illinois). At the time of injection, the suspended cells had an average radius of  $7.0 \pm 0.5 \mu$ m (Supplemental Figure 2). The chamber was incubated overnight (12-16 hours) at  $37^\circ\text{C}$  and 5%  $\text{CO}_2$  in a humidified environment to allow the cells to become adherent to the base of the chamber.

### Fluorescence Microscopy

Widefield fluorescence imaging was performed on a DMI6000B (Leica Microsystems, Bannockburn, Illinois) equipped with a  $63\times/0.7$  HC PL Fluotar L objective and a  $20\times/0.4$  HCX PL FLUOTAR objective, L5 (Ex 480/40; Em 527/30) and Y3 (Ex 545/25; Em 605/70) filter cubes (all from Leica Microsystems), and a CM-9100-02 EMCCD camera (Hamamatsu Photonics, K.K. Shizuoka Pref, Japan). Confocal fluorescence imaging was performed on an LSM 800 (Carl Zeiss Microscopy, LLC, Thornwood, New York) using a  $63\times/1.4$  Plan Apochromat M27 oil immersion objective. 353 and 488 nm lasers were used for

excitation with detection wavelength bands of 400 nm to 490 nm for the NucBlue stain and 490 nm to 617 nm for the Cell-Tracker stain, respectively. Z-stacks of confocal images of cells adherent to the base of the chamber were obtained at a z resolution of  $0.37 \mu$ m, with each image measuring  $100 \mu\text{m} \times 100 \mu\text{m}$  ( $1000 \text{ pixels} \times 1000 \text{ pixels}$ ).

### Fluorescence Calibration

Microfluidic chambers seeded the night before in NucBlue-containing medium as previously described were used to characterize the relationship between Pro concentration and fluorescence intensity. Chemical permeabilization experiments were performed in microfluidic chambers using a solution of 0.1% (v/v) Triton-X100 (Sigma, St. Louis, Missouri) with Pro (0, 1.5, 3, 7.5, 15, 30, 75, and 150  $\mu\text{mol/L}$ ; ThermoFisher Scientific) in PBS introduced into the chamber using a 1-mL syringe and 24 AWG PTFE tubing. Images were obtained using the widefield fluorescence microscope described previously 5 minutes following permeabilization using a  $20\times$  objective with exposures of 20 milliseconds, once the fluorescence intensity in the chamber had stabilized (data not shown). Five images were obtained at each Pro concentration and each exposure using a  $2 \times 2$  binning scheme. Chemical permeabilization treatments were performed 3 times for each treatment condition and included more than 30 cells in each replicate for the condition. These data indicated that an extracellular Pro

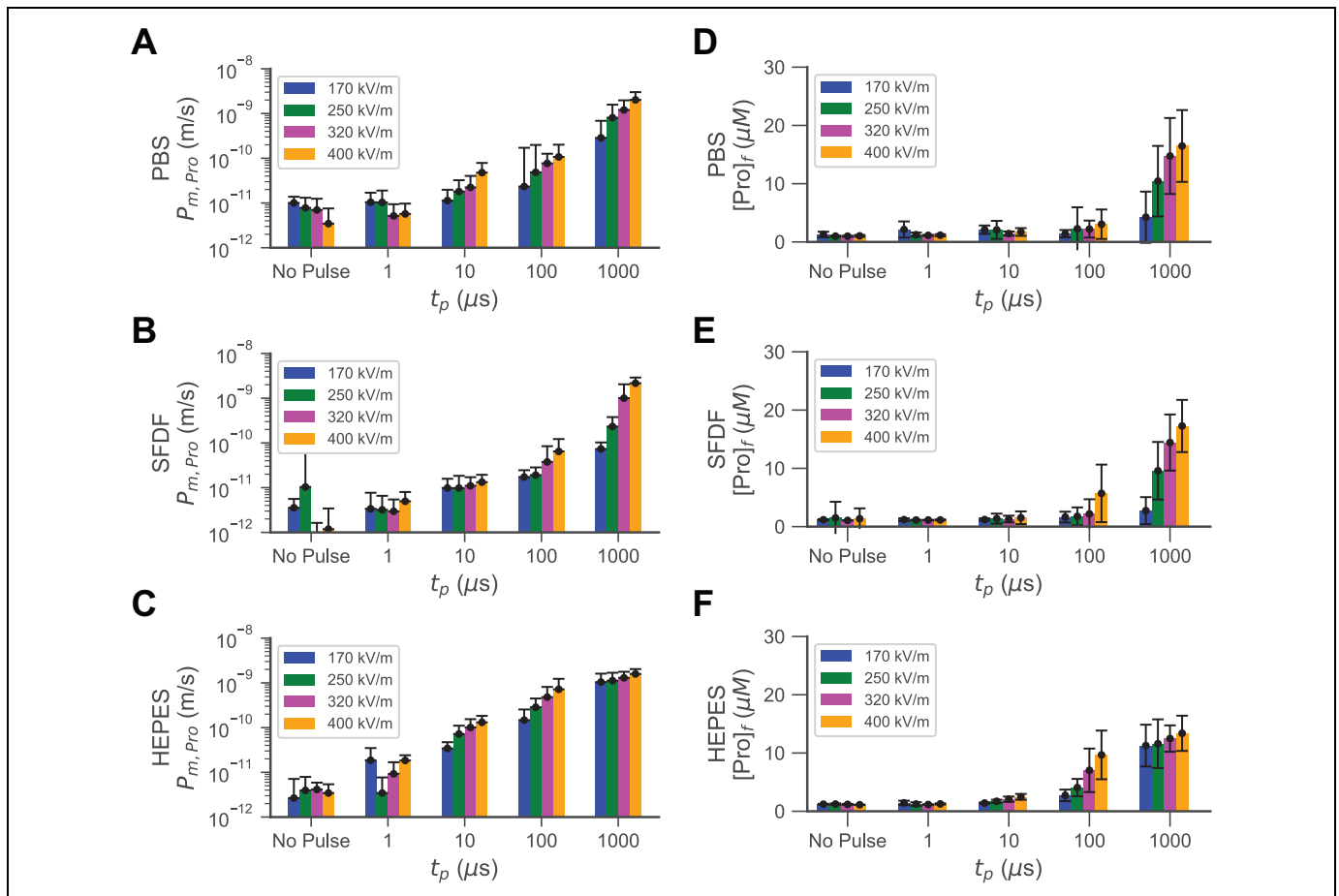


**Figure 3.** The cell membrane permeability to Pro,  $P_{m,Pro}$  (log-scale), and the final Pro concentration 30 minutes following pulse application  $[Pro]_f$  (linear-scale) increase with increasing pulse duration and electric field strength in each buffer. The permeability immediately following PEF application is calculated according to Equation 1 for 3 different medium compositions: (A) PBS, (B) SFDF, and (C) HEPES. The average diffusive permeability of the cell membrane  $P_{m,Pro}$  is averaged over the first 3 minutes of observation and presented as a function of pulse duration  $t_p$  and amplitude. Error bars are shown in only the positive direction due to the logarithmic scale on the vertical axis and represent the standard deviation. The total uptake of Pro 30 minutes following PEF application increases dramatically between pulse durations of 100 to 1000  $\mu s$  and  $E \geq 320$  kV/m for cells immersed in D, PBS, E, SFDF, and F, HEPES. The final concentration of intracellular Pro  $[Pro]_f$  measured 30 minutes following PEF applications is presented as a function of pulse duration  $t_p$  and amplitude. Error bars represent standard deviation. Numerical values are given in Supplementary Tables 1 to 3. Pro indicates propidium; PEF, pulsed electric field; PBS, phosphate-buffered saline; SFDF, serum-free DMEM/F12 medium.

concentration of 30  $\mu mol/L$  at an exposure of 20 milliseconds would allow free Pro ions to enter the cell, bind to double-stranded nucleic acids, and remain below the saturation limit of the imaging system (Supplemental Figure 3D). The fluorescence intensity–concentration calibration relationship was determined to be  $I = 700[Pro]$ , where  $I$  is the fluorescence intensity and  $[Pro]$  is given in  $\mu mol/L$ , with a Pearson  $r$  value of  $r = 0.63$  and corresponding  $p$  values of  $p = 2.0 \times 10^7$ . This calibration provides a correlation between the bound intracellular concentration of Pro and the cytosolic concentration of Pro at equilibrium.

### Application of PEFs

Electric field pulses were applied to the cells in the microfluidic chamber through stainless steel electrodes (0.18 mm

diameter) inserted into the tubing at the inlet and outlet of the chamber. Immediately prior to PEF application, cells were immersed in 1 of 3 buffer solutions: phosphate-buffered saline (PBS) containing 30  $\mu mol/L$  Pro (ThermoFisher) with no calcium and magnesium, phenol-free serum-free culture medium (SFDF) 1:1 Dulbecco modified Eagle’s medium (DMEM)/F12 (Gibco) containing 1% penn/strep and 30  $\mu mol/L$  Pro, or a low-conductivity, calcium-free medium containing 10 mmol/L HEPES (Sigma), 250 mmol/L sucrose (Fisher Scientific, Pittsburgh, Pennsylvania), 7.5 mmol/L NaCl (Fisher Scientific), and 30  $\mu mol/L$  Pro. The pH of each buffer was adjusted to 7.2 using HCl and NaOH. The electrical conductivities of the buffers were 1.01, 0.93, and 0.08 S/m for the PBS, SFDF, and HEPES, respectively, while their respective osmolarities were 278, 306, and 310 mOsmol/L. No significant cellular swelling was immediately observed upon addition of any of the buffer

solutions in the absence of PEFs. An electrical amplifier based on an H-bridge topology was used to deliver a 3 kV electrical pulses across the length of the chamber. A function generator (SDG 5082, Siglent, Solon, Ohio) was used to trigger the amplifier, and the output voltage was monitored using a high-voltage probe (BTX High-Voltage Probe, Harvard Apparatus, Holliston, Massachusetts) connected to an oscilloscope (DS1104, RIGOL Technologies Inc, Beaverton, Oregon). The anode of the amplifier output was always positioned at the wide inlet of the chamber. The PEFs were applied using a single pulse with 4 durations. Electrical pulses were always applied as a single 1-, 10-, 100-, or 1000-microsecond pulse (Supplemental Figure 1), as measured from the initialization of the rising edge of the pulse to the initialization of the ringing on the falling edge of the pulse. Images following the pulse application were obtained within 15 seconds of completion of the application and once every minute for the following 30 minutes. Each electric field strength and pulse duration was tested on subpopulations of cells ( $n = 27$ -114 cells) in 3 individual chambers.

Worst-case analysis of the Joule heating concomitant with pulse applications indicates that the Joule heating during a 1000-microsecond pulse in PBS and SFDF induced a  $>19^{\circ}\text{C}$  temperature increase above room temperature ( $22^{\circ}\text{C}$ ), neglecting any thermal losses. For the experiments involving cells in the HEPES buffer and the experiments involving cells in the PBS and SFDF exposed to a 1-, 10-, and 100-microsecond pulse, temperature increases of  $<5^{\circ}\text{C}$  was observed, which is well below the threshold of thermal damage for all other conditions (Supplemental Figure 4).

The electric field strengths at each position in the chamber were 170, 250, 320, and 400 kV/m as estimated from the chamber position (Figure 1D-F). While the ringing shown in Figure 2 is shown for a chamber containing PBS, the ringing was of amplitudes approximately  $\pm 3$  kV beyond the 3 kV set voltage (Supplemental Figure 1) and durations on the order of a microsecond for pulses applied to chambers containing each of the 3 buffers investigated. This ringing was unintended and thought to be due to the high-voltage generator discharging through the large resistance of the microdevice ( $\gg 1$  k $\Omega$ ). It has been previously shown that the length of time the transmembrane potential exists beyond the strength–duration EP threshold governs permeabilization for cells exposed to PEFs, with a 10% sinusoidal amplitude modulation having little impact on the thresholds at which cells become permeabilized.<sup>17,27</sup> The ringing present on the rising and falling edges of each pulse in the present case was present for  $\leq 50\%$  of the total pulse duration for all but the 1-microsecond pulse, and therefore we anticipate that this ringing will not dramatically impact these results. These waveforms are functionally similar to a high-amplitude pulse followed by a longer low-amplitude pulse, which has been shown to enhance molecular delivery by first permeabilizing the membrane then electrophoretically driving the charged molecules into its interior.<sup>28</sup> Therefore, we anticipate any deviation of the data herein to overpredict the permeability induced by a similar duration square pulse.

## Image Processing

Image files were parsed using FIJI (version 2.0.0-rc-43/1.51d).<sup>29</sup> Batch image processing was performed on each stack of images at each time point and each position with the chamber using CellProfiler (v2.2.0).<sup>30</sup> First, edge detection was performed on the blue channel (NucBlue channel) of each image set using a Sobel filter, and the nuclei in the resulting images were identified and characterized, including its circularity and area. The nuclear outlines generated from the blue channel were mapped to the red channel (Pro channel), and the mean intensity of the nuclei in the red channel was measured and recorded at each point in time for each experimental condition.

Image stacks were reconstructed in 3-D Slicer (v4.6.2),<sup>31</sup> imported into MeshLab (v2016.12),<sup>32</sup> and cleaned to remove isolated edges and vertices and close holes to make the mesh watertight. All curve fitting was performed using the Scipy module (v1.0.1) in Python 3.6.5. The surface area and volume of each cell was then calculated from these reconstructions. The mean and standard deviations of the cell surface area and volume ( $n = 56$  cells) were plotted as histograms and against each other (Supplemental Figure 3A and B). The Pearson's  $r$  for the best-fit regression line was  $r = 0.71$ , corresponding to a  $p$  value of  $p = .049$ , indicating a good linear fit by the line  $A = k_0V + k_1$ , where  $A$  and  $V$  are the cellular surface area and volume, in  $\mu\text{m}^2$  and  $\mu\text{m}^3$ , respectively, and  $k_0 = 1.2 \mu\text{m}^{-1}$  and  $k_1 = -390 \mu\text{m}^2$  are the constants that describe the statistical best-fit line (Supplemental Figure 3C).

## Quantitative Calculation of Pro Uptake

Previously, the diffusive permeability of the cell (herein referred to as permeability) has been shown to depend on the duration and degree of permeabilization of the membrane.<sup>10,17,27</sup> To measure permeability, time lapse microscopy was used to observe the fluorescence intensity of the nuclei of CHO-K1 cells in a microfluidic chamber (Figure 1). To ensure camera settings did not interfere with these correlations, calibrations were performed under imaging conditions under which fluorescence intensity of fluorescence signals did not saturate the camera sensor anywhere in the image.

The nucleus was selected for observation using Pro as its fluorescence signal is brighter than the fluorescence signal from Pro in the cytosol due to the abundance of nucleic acids therein. In order to make our results quantitative, the average cell volume and surface area were determined. We experimentally established the relationship between the fluorescence of bound Pro within a cell's nucleus and the cytosolic Pro ( $[\text{Pro}]_{\text{cyt}}$ ) by developing standard curves. To obtain these curves, we chemically permeabilized cells in the presence of increasing fixed extracellular concentrations of Pro. Extracellular Pro concentrations were selected to be well below those determined to saturate the binding sites in the nucleus (Supplemental Figure 3D). Therefore, our calibration provided an estimate of intracellular Pro as a function of the fluorescence intensity of the bound Pro in the nuclei of permeabilized cells,

based on the expectation that their interiors are well mixed,<sup>33</sup> and binding occurs rapidly.<sup>34</sup>

This assumption of a well-mixed intracellular space is supported by many previous reports, where the fluorescence of Pro and similar molecules are used as surrogates to assess the diffusive transport into the cells. It has been shown that Pro-mediated intracellular fluorescence is able to reach its peak intensity approximately 2 seconds following the delivery of an electrical pulse 100-fold longer than the maximum used in the present work.<sup>22</sup> Furthermore, it was noted that Pro is able to enter the cell, bind to nucleic acids in the cytosol, and become fluorescent in 60 microseconds, indicating that the binding process alone requires <60 microseconds to occur.<sup>35</sup> Similarly sized molecules have also been shown to readily and rapidly diffuse throughout the cell and cross the nuclear membrane after being microinjected into the cytoplasm.<sup>36,37</sup> These measurements indicate that Pro is able to enter the cell, bind to nucleic acids, and become fluorescent within a time period tens- to thousands-fold shorter than the timescale of the 60-second interval between consecutive images we employ here. Furthermore, the fluorescence intensity of the Pro-bound nucleic acids outside the nucleus contributes a negligible integrated fluorescence intensity compared to those within due to the larger concentration of double-stranded nucleic acids it contains.<sup>23,38</sup> We assume that the cell interior is well mixed and the bound Pro is close to equilibrium with cytosolic Pro, and we therefore approximate the fluorescence intensity of the nucleus as reflective of the unbound Pro within the cell.

For the present study, a negligible pressure gradient existed across the cells in the microfluidic chamber.<sup>15,20,21</sup> Electrophoretic forces were neglected, and the total flux of free Pro was considered purely diffusive  $J_{\text{Pro}}(t) \approx \Delta(V[\text{Pro}(t)])/(A\Delta t)$ ,<sup>23,37,39</sup> where  $[\text{Pro}]$  refers to the concentration of intracellular unbound Pro. By determining the intracellular change in unbound Pro concentration over time ( $\Delta[\text{Pro}]/\Delta t$ ) and treating the cell area and volume as constants, the permeability of the cell membrane  $P_{\text{m,Pro}}(t)$  may be estimated as:

$$P_{\text{m,Pro}}(t) = \left( \frac{V}{A\Delta t} \right) \left( \frac{[\text{Pro}(t + \Delta t)] - [\text{Pro}(t)]}{[\text{Pro}]^{\text{ext}} - [\text{Pro}(t)]} \right), \quad (1)$$

where  $P_{\text{m,Pro}}(t)$  is the membrane permeability,  $V$  and  $A$  are the volume and surface area of an average cell, respectively, and  $[\text{Pro}]^{\text{ext}} = 30 \mu\text{mol/L}$  is the external concentration of Pro.  $\Delta[\text{Pro}] = [\text{Pro}(t + \Delta t)] - [\text{Pro}(t)]$  and  $\Delta t$  are the change in Pro concentration and time, respectively, between 2 consecutive images in a time series. The slope  $\Delta[\text{Pro}(t)]/\Delta t$  was calculated numerically using a forward finite difference scheme between an image and the one immediately after it. The fluorescence intensity of the nuclei in each image was averaged, and  $P_{\text{m,Pro}}(t)$  was calculated using the image and the subsequent image in the series. A linear fit was performed for the first 3 minutes of each  $[\text{Pro}(t)]$  curve, and the slope of this line was used to approximate its initial slope  $\Delta[\text{Pro}(t)]/\Delta t$ . Then, the permeability of the cell membrane to Pro was calculated using Equation 1 (Supplemental Tables 1-3).

To ensure that our calculations are consistent with these assumptions, the mass transfer Biot number  $Bi_m$  was used to characterize the ratio of fluidic resistance of Pro across the cell membrane compared to the fluidic resistance Pro in the aqueous intracellular and extracellular environments.  $Bi_m = LP_{\text{m,Pro}}/D_{\text{Pro}}$ , where  $L = V/A \approx 1 \mu\text{m}$  is the characteristic length of the cell expressed as the ratio of the volume of a cell  $V$  to its surface area  $A$  and  $D_{\text{Pro}} \approx 5.3 \times 10^{-13} \text{ m}^2/\text{s}$  is the diffusion coefficient of Pro and similarly sized solutes inside the cell.<sup>21,33,36,40-42</sup> Imposing  $Bi_m \leq 1$  indicates that the transport across the cellular membrane is slow compared to the diffusion on its interior and exterior. From this calculation,  $P_{\text{m,Pro}} < 5.3 \times 10^{-7} \text{ m/s}$  in order to make the well-mixed approximation. The maximum values we estimate for  $P_{\text{m,Pro}}$  are as high as  $1.3 \pm 0.4 \times 10^{-8} \text{ m/s}$  (Supplemental Tables 1-3), indicating that this assumption is valid, and we consider the intracellular space well mixed and close to diffusive equilibrium.

Although we have presented quantitative estimates of the cell membrane's diffusive permeability to Pro ( $P_{\text{m,Pro}}$ ), we must specify the appropriate context and scope of our analysis. The resolution limit of the 14-bit camera is approximately  $0.001 \mu\text{mol/L}$  under these conditions. To quantify the reliable resolution for our measurements using Equation 1, we set the smallest possible value between 2 consecutive time point measurements (on the order of minutes) and selected the concentration  $[\text{Pro}](t \sim 0) = 0$  to give the worst-case resolution of our diffusive permeability calculation as approximately  $P_{\text{m,Pro}} \approx 1 \times 10^{-12} \text{ m/s}$  during the first few seconds to minutes following PEF application. We note that the low resolution of our determination at later time points made it difficult to quantify the membrane permeability at these times. Below these limits, it is possible that a membrane had become permeable, but to a degree less than the resolution of our analysis would allow and would be considered impermeable. Further, the untreated controls are all at or below the resolution threshold in all measurements, indicating that they are below the threshold for reliable quantification of Pro uptake.

## Results

### Total Pro Uptake and Permeability Increase With Applied Energy

To efficiently measure membrane permeability, our microfluidic chamber was designed to enable simultaneous measurements of the cellular response to 4 electric field strengths. By acquiring images at 2, 4, 6, and 8 mm along the long axis of the chamber (Figure 1), cells exposed to 4 electric field strengths could be monitored in a single experiment. We emphasize that the electric field strengths presented are approximate representations of the applied electric field, obtained under electrostatic assumptions and modeled using an idealized square waveform. In order to ensure that our observations were robust to variability in medium composition, we performed experiments in PBS, SFDF, and a low-conductivity HEPES buffer containing

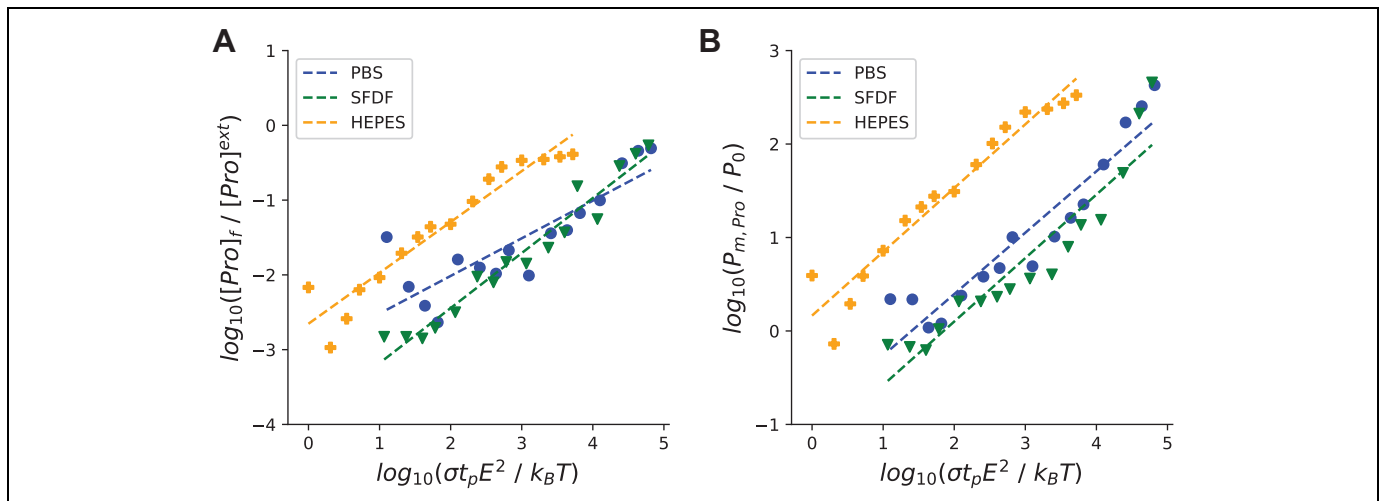


**Figure 4.** The log of the final concentration of Pro inside a cell after pulse application (A) and the initial membrane permeability (B) are strongly correlated to the log of the applied energy. A, The ratio of the intracellular Pro concentration 30 minutes after treatment to the extracellular Pro concentration (30  $\mu\text{mol/L}$ ) is plotted against the log of the applied energy  $\sigma t_p E^2$ , normalized to the product of the Boltzmann constant and the ambient temperature (22°C). The best-fit lines are  $y = 0.5x - 3.0$  for PBS ( $p < .001$ ),  $y = 0.74x - 3.9$  for SFDF ( $p < .001$ ), and  $y = 0.68x - 2.7$  for HEPES ( $p < .001$ ), where  $y$  is the vertical coordinate and  $x$  is the horizontal coordinate. B, The log of the membrane permeability within the first 3 minutes following pulse application ( $P_{m,\text{Pro}}$ ), relative to the untreated control membrane permeability ( $P_0 = 4.7 \times 10^{-12}$  m/s), is plotted against the log of the applied energy normalized to the Boltzmann constant and the ambient temperature (22°C). The best-fit lines are  $y = 0.66x - 0.9$  for PBS ( $p < .001$ ),  $y = 0.68x - 1.3$  for SFDF ( $p < .001$ ), and  $y = 0.68x + 0.2$  for HEPES ( $p < .001$ ), where  $y$  is the vertical coordinate and  $x$  is the horizontal coordinate. For each linear fit, Pearson  $r$  was determined for each correlation and the  $P$  values reported apply to each of the traces individually. Pro indicates propidium; PEF, pulsed electric field; PBS, phosphate-buffered saline; SFDF, serum-free DMEM/F12 medium.

sucrose to balance its osmolarity to a physiological range (approximately 300 mOsm/L). The intracellular–extracellular concentration gradient of Pro persists beyond 30 minutes following application for all experimental conditions.

In Figure 3, it is clear that the 100- and 1000-microsecond pulses greatly increased the permeability for cells in each application buffer. Additionally, the molecular uptake of Pro 30 minutes after application was greatly enhanced over the controls (Figure 3D–F). The initial permeabilities showed little difference between PBS and SFDF (Figure 3A and B). However, cells in HEPES became permeabilized at lower strength–duration thresholds (Figure 3C). The population response of cells treated in the low-conductivity HEPES buffer was more uniform at each electric field strength and across pulse durations (Figure 3). We conclude that membrane resealing governs the decrease in molecular uptake over the minutes following PEF application before diffusive equilibrium is established (Figure 3).

Our data suggest a strong correlation between the logarithm of the final concentration of Pro for cells and the logarithm of the applied energy for each of the buffers (Figure 4A). This is in good agreement with the previous literature,<sup>43–46</sup> which suggests that membrane permeability increases according to power relationships between pulse duration and number and the induced membrane permeability (Figure 4B). In order to quantify these relationships, intracellular Pro, membrane permeability, and applied energy were normalized. The energy applied through electrical pulses ( $\sigma t_p E^2$ ) was normalized to the Boltzmann constant ( $k_B$ ) and the ambient temperature ( $T = 295$  K).

Membrane permeability was normalized to the permeability of the untreated controls ( $P_0 = 4.7 \times 10^{-12}$  m/s), and the concentration of Pro within the cells 30 minutes following treatment was normalized to the external Pro concentration ( $[\text{Pro}]^{\text{ext}} = 30 \mu\text{mol/L}$ ). The base-10 logarithms of each of these parameters were fit using a linear fit for each of the buffers with Pearson  $r$  used to quantify linearity. The logarithm of the Pro uptake was found to be linearly related to the logarithm of the applied energy with a slope of 0.5 and an intercept of  $-3.0$  for cells in PBS ( $p < .001$ ), a slope of 0.74 and an intercept of  $-3.9$  for cells in SFDF ( $p < .001$ ), and a slope of 0.68 and an intercept of  $-2.7$  for cells in HEPES ( $p < .001$ ; Figure 4A). The logarithm of permeability was found to be linearly related to the logarithm of the applied energy with a slope of 0.66 and an intercept of  $-0.9$  for cells in PBS ( $p < .001$ ), a slope of 0.68 and an intercept of  $-1.3$  for cells in SFDF ( $p < .001$ ), and a slope of 0.68 and an intercept of 0.2 for cells in HEPES ( $p < .001$ ; Figure 4B). Interestingly, the slope of the best-fit lines appears to be parallel, with a slope of approximately 0.7.

### Slow Uptake Rates Correlate With Smaller Pulse Strengths

Following PEF application, we observed a subpopulation of cells exhibiting a prolonged uptake of Pro sufficient to achieve an intracellular concentration of 25% of the external Pro concentration after 30 minutes (Figure 5A). This is an important



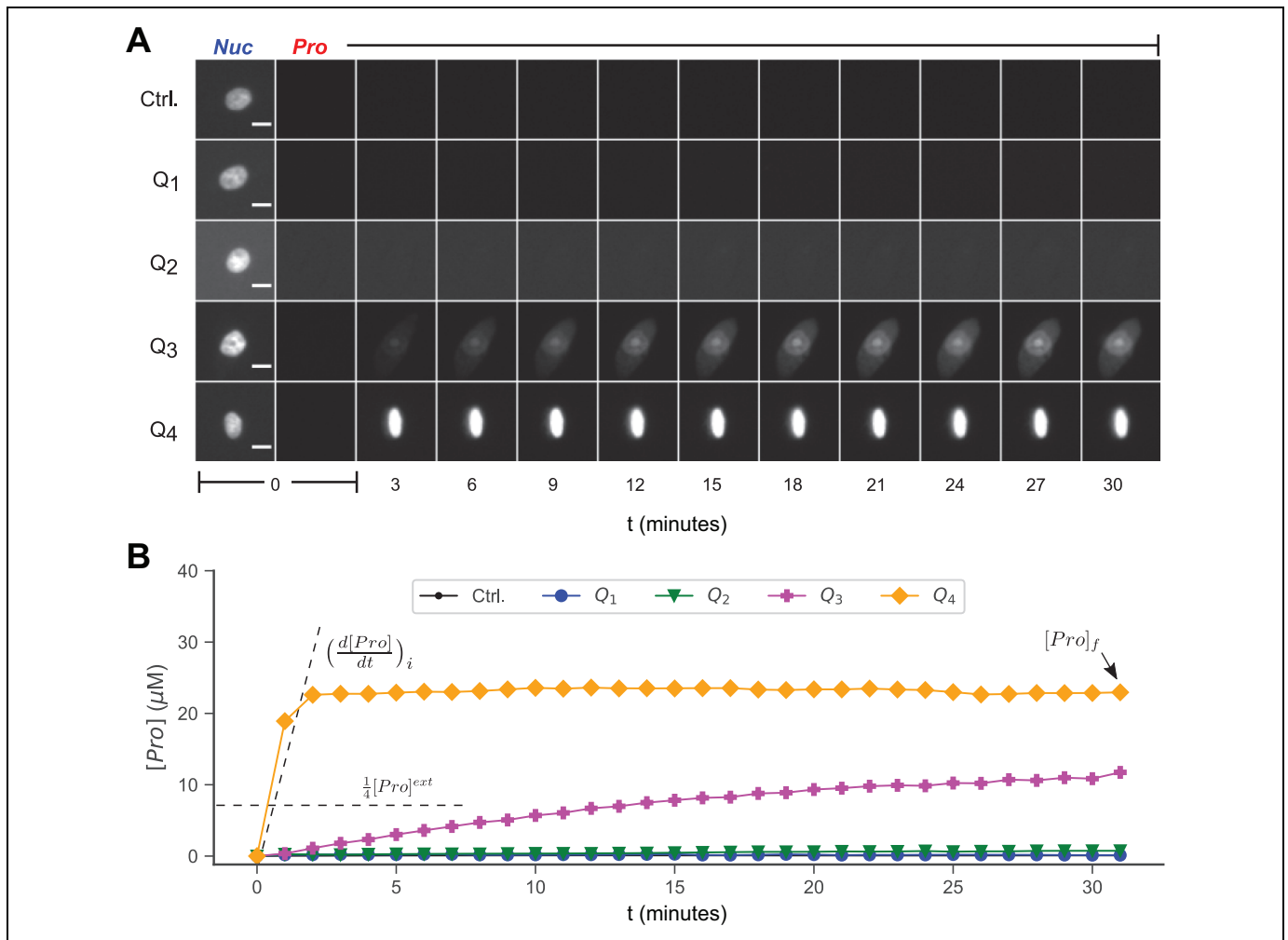


**Figure 5.** The intracellular concentration of Pro ( $[Pro]$ ) is presented as a function of time  $t$  for each image during the imaging period (30 minutes). A, Time series images show uptake responses of single cells to a single electrical pulse as Pro enters cells at different rates. Nuclei are shown stained with NucBlue (Nuc; 10  $\mu\text{m}$  scale bar) and Pro in the pre-treatment images and Pro alone in the remainder of the images. Control images are indicated by Ctrl. B, A cell's behavior is shown as 1 of 4 responses based on the time when the Pro fluorescence in the nucleus reached its half-maximal concentration and the final concentration of intracellular Pro. A cell was classified as  $Q_1$  if  $t_{1/2} < 5$  minutes and  $[Pro]_f < 7.5 \mu\text{M}$ . The  $Q_2$  subpopulation is based on  $t_{1/2} \geq 5$  minutes.  $Q_3$  is based on  $[Pro]_f \geq 7.5 \mu\text{M}$  and  $t_{1/2} \geq 5$  minutes.  $Q_4$  corresponds to  $[Pro]_f \geq 7.5 \mu\text{M}$  and  $t_{1/2} < 5$  minutes. Uptake profiles are derived from the individual cells in (A) and show their individual Pro uptake responses over time. Untreated control data are indicated by Ctrl. Pro indicates propidium.

basic finding. To identify this subpopulation, we calculated the final concentration of Pro inside the cell after 30 minutes ( $[Pro]_f$ ) and the time at which the intracellular concentration reached half this value ( $t_{1/2}$ ). For each cell, ( $t_{1/2}$ ,  $[Pro]_f$ ) was determined and plotted for each pulse duration and electric field strength combination (Figure 5). Previous reports indicate that a delay of approximately 300 seconds may exist between the time of PEF application and significant permeabilization.<sup>20,21,47</sup> Therefore, the cutoff of 5 minutes was used to discriminate between cells with overall slow rates of Pro uptake and those with more rapid uptake rates. Upon inspection, a threshold of 25% of the extracellular Pro concentration ( $[Pro]^{ext}/4 = 7.5 \mu\text{mol/L}$ ) was selected to discriminate between cells allowing large or small quantities of Pro through the membrane.

This analytical scheme created 4 quadrants in the ( $t_{1/2}$ ,  $[Pro]_f$ ) space (Figure 6). The lower left quadrant is labeled  $Q_1$  and corresponds to subpopulation of cells that reach their  $[Pro]_f$  quickly but ultimately have  $[Pro]_f < [Pro]^{ext}/4$ . The lower right quadrant is labeled  $Q_2$  and corresponds to the subpopulation of cells for which  $[Pro]_f < [Pro]^{ext}/4$  and  $t_{1/2} \geq 5$  minutes. The upper right quadrant is labeled  $Q_3$  and corresponds to the subpopulation of cells for which  $[Pro]_f \geq [Pro]^{ext}/4$  and  $t_{1/2} \geq 5$  minutes. The upper left quadrant is labeled  $Q_4$  and corresponds to the subpopulation of cells for which  $[Pro]_f \geq 7.5 \mu\text{mol/L}$  and reached  $t_{1/2} < 5$  minutes. At high electric field strengths and long pulse durations, cellular behavior is relatively homogeneous, with Pro rapidly entering nearly all cells rapidly after PEF application.  $Q_1$  and  $Q_2$  describe the behavior of

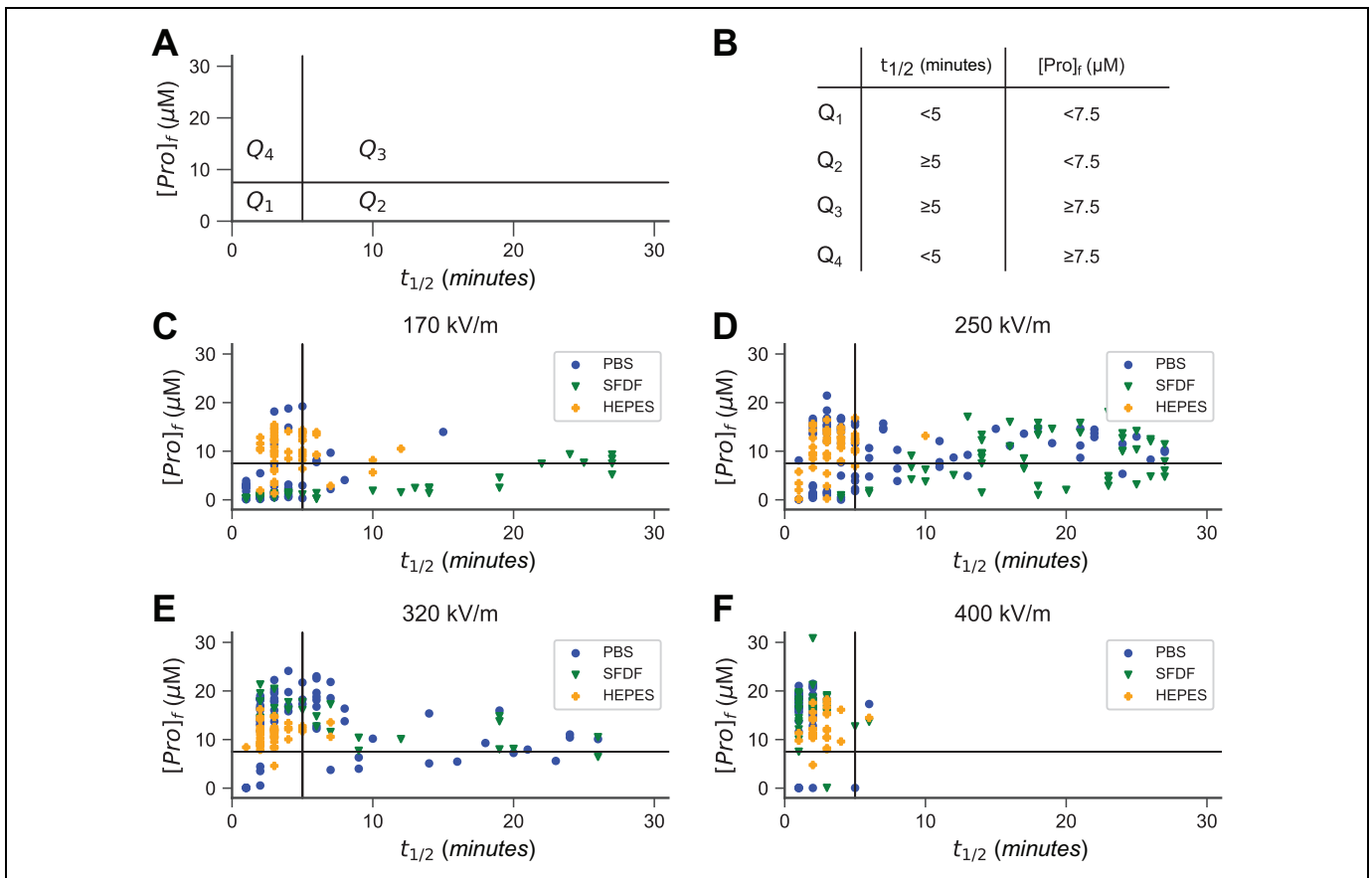


**Figure 6.** As the electric field strength increases, the fraction of cells in the  $Q_1$  and  $Q_2$  subpopulations decrease. Subsequently, a subpopulation with slow but more Pro uptake emerges ( $Q_3$ ; upper right quadrant). At even larger  $E$ , most cells are part of the subpopulation exhibiting rapid Pro uptake ( $Q_4$ ; upper left quadrant). A, Cellular response was quantified based on the final concentration of Pro 30 minutes postapplication ( $[\text{Pro}]_f := [\text{Pro}](t = 30 \text{ minutes})$ ) and the time at which each cell reached its half-final concentration ( $[\text{Pro}](t_{1/2}) := [\text{Pro}]_f/2$ ). B, Criteria for each quadrant are based on whether the Pro uptake of a cell 30 minutes following PEF treatment is  $[\text{Pro}]_f \geq [\text{Pro}]^{\text{ext}}/4$  (horizontal lines) and whether the cell achieved  $[\text{Pro}]_f/2$  within 5 minutes of PEF treatment ( $t_{1/2} < 5$  minutes). The data shown are for a single 1000  $\mu\text{s}$  pulse at C, 170 kV/m, D, 250 kV/m, E, 320 kV/m, and F, 400 kV/m. Pro indicates propidium; PEF, pulsed electric field.

cells exhibiting minimal Pro uptake, regardless of whether the response is rapid ( $Q_1$ ) or prolonged ( $Q_2$ ). Cells in the  $Q_3$  subpopulation,  $t_{1/2} \geq 5$  min but eventually reach relatively large intracellular Pro concentrations compared to  $Q_1$  and  $Q_2$  cells ( $[\text{Pro}]_f \geq [\text{Pro}]^{\text{ext}}/4$ ).  $Q_3$  cells exhibit a large transient Pro uptake or experience a delay before becoming significantly permeabilized. The  $Q_4$  subpopulation experiences a large, rapid influx of Pro. Across PEF application parameters and buffers, the  $Q_2$  and  $Q_3$  subpopulations appear to be intermediate responses between no EP and EP (Figure 7). Many of the cells exhibiting a prolonged Pro uptake ( $Q_3$ ) have a similar  $[\text{Pro}]_f$  compared with the subpopulation in  $Q_4$  but with slower uptake rates and occur at lower strength–duration PEF thresholds. At the largest electric field strengths and longest pulse durations, the  $Q_3$  subpopulation decreases and cells become more concentrated in the  $Q_4$  subpopulation (Figure 6).

## Discussion

Microfluidic devices have been long used to investigate cellular EP and enable the interrogation of single cells using electric fields in a tightly controlled environment.<sup>48</sup> Here, the development of a microfluidic chamber that enables the effects of PEFs on many cells to be studied simultaneously was instrumental in efficiently performing the experiments presented. By simultaneously exposing cells in different locations along the length of the chamber to different electric field strengths, we were able to observe 4 groups of cells exposed to different electric field strengths at the same time. Technologies such as flow cytometry are able to assay a larger population of cells but require them to be suspended and do not allow the same cells to be tracked between consecutive time points. Our microdevice design provided a more time-efficient method for studying the cellular response to EP than in conventional setups that use 2 parallel plate or needle electrodes. The chamber design was integrated with standard fluorescence microscopy equipment

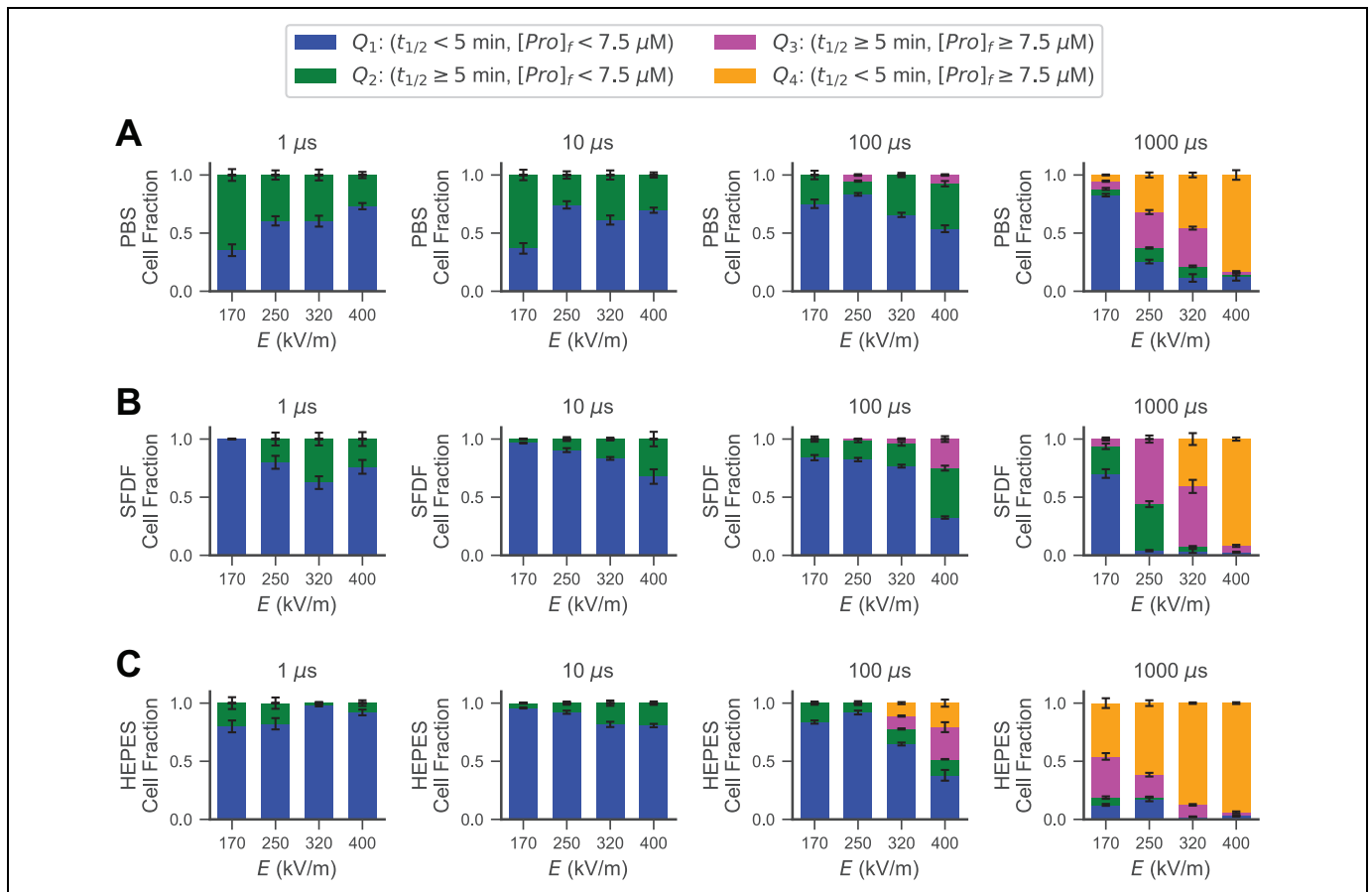


**Figure 7.** At electric field strengths and durations below the threshold for rapid Pro uptake, cells exhibit a prolonged uptake response that renders them sufficiently permeable to allow significant molecular transport. Data are shown for cells immersed in each experimental buffer: A, PBS, B, SFDF, and C, HEPES. Each of the cell populations treated at a given pulse duration are split into 4 classifications:  $Q_1$ ,  $Q_2$ ,  $Q_3$ , and  $Q_4$ . At shorter pulse durations (1-100 microseconds), the majority of cells contain relatively little Pro ( $Q_1$  and  $Q_2$  subpopulations). Larger  $Q_3$  subpopulations are generated at intermediate pulse durations and strengths (320-400 kV/m with a 100  $\mu s$  pulse; 170-400 kV/m with a 1000  $\mu s$  pulse) and begin to become detectably permeabilized with  $[Pro] \geq [Pro]^{ext}/4$  30 minutes after PEF application, but with a slower, more gradual uptake rate ( $t_{1/2} \geq 5$  minutes). Finally, at the longest pulse durations and largest electric field strengths, the  $Q_4$  subpopulation contains the majority of the cells that facilitate fast rates of significant Pro uptake ( $[Pro]_f \geq [Pro]^{ext}/4$ ;  $t_{1/2} \leq 5$  minutes) through large cell membrane permeabilities up to  $1.3 \pm 0.4 \times 10^{-8}$  m/s. The total cell population is presented as a sum of the fractional contributions from the  $Q_1$ ,  $Q_2$ ,  $Q_3$ , and  $Q_4$  subpopulations. Error bars represent standard error and each column represents between 27 and 114 cells (62 average). Pro indicates propidium; PBS, phosphate-buffered saline; PEF, pulsed electric field; SFDF, serum-free DMEM/F12 medium.

and allowed adherent cells to be tracked and analyzed individually over time.

We present estimates of the cell membrane permeability to Pro using measurements of the uptake rate into the cell using our microfluidic chamber. We show that a single 1000-microsecond electrical pulse at 400 kV/m can induce permeabilities of  $1.3 \pm 0.4 \times 10^{-8}$  m/s to Pro, which is similar in size to adenosine triphosphate (ATP) but has a larger charge magnitude. Comparable permeabilities ( $\sim 6 \times 10^{-9}$  m/s assuming a similar  $V/A$  ratio) have been induced for ATP by ten 100-microsecond or ten 1000-microsecond pulses in the same cell line and result in an ATP loss of 0.050 to 0.80 nmol/min with 120 to 400 nmol total ATP leakage.<sup>1</sup> Eight-pulse PEFs with amplitudes 80 to 120 kV/m have been shown to deplete cells of 50% to 95% of their intracellular ATP<sup>49-51</sup> and lead to a 25% to 50% decrease in

cell viability in the presence of 1 to 3 mmol/L extracellular calcium.

At least 2 mechanisms could drive this loss of cell viability: ATP leakage and ATP depletion, although other physical and biochemical mechanisms could very well be implicated.<sup>7,52</sup> Toward the former, approximately  $5 \times 10^{-6}$  nmol ATP is present within a typical mammalian cell.<sup>53-55</sup> With similar permeabilities of the cell membrane to ATP as those observed here for Pro, it may be possible to deplete cells within a given treatment volume of more than 25% of their intracellular ATP using a single electrical pulse.

With regard to the ATP depletion, it has been hypothesized that the entry of exogenous calcium requires a cell to expend more ATP on calcium pumps to reestablish cellular homeostasis, potentially leading to its demise.<sup>49-51,56</sup> Although these estimates of ATP depletion and calcium leakage occur on

different timescales with different pulse parameters in previous reports, the estimates of  $P_{m,Pro}(t)$  provided in part I of this report serve as a lower bound for quantitative estimates of calcium permeability, which has a similar charge and a diffusion coefficient approximately 2.5 times greater than that of Pro in water.<sup>57</sup> These estimates provide a heuristic context for the present work and indicate that it may be possible to take advantage of both of these mechanisms using single-pulse PEF application with a calcium adjuvant in order to decrease intracellular ATP and inhibit cellular recovery.

Other potential mechanisms of cellular damage have been reported, including lipid peroxidation, the formation of reactive oxygen species, and metabolic thermal damage.<sup>58</sup> We note that bleb formation along the cell membrane and inflection points in the Pro uptake profile<sup>20,21,47</sup> were observed (data not shown). These observations and the prolonged Pro uptake of the subpopulation of cells in  $Q_3$  could implicate the presence of reactive oxygen species in the mechanism driving membrane injury.<sup>59</sup> Permeabilization is no doubt impacted by the temperature increase of greater than 19°C of the solution within the chambers containing PBS and SFDF for the 1000-microsecond pulse case (Supplemental Figure 4). It is likely our observations still hold in the presence of such effects as these temperatures must be sustained for minutes for observable damage to occur.<sup>58</sup> However, further investigations will be required to elucidate the quantitative relationship between membrane permeability and cell viability.

Our data show a subpopulation of cells that experience significant Pro uptake at lower electric field strength–duration thresholds than the general population ( $Q_3$ , Figure 7). Due to the relatively long delay (3–10 minutes) between PEF application and the increase in Pro uptake, this phenomenon may be a biological or biochemical response. The  $Q_3$  subpopulation appeared at strength–duration thresholds lower than required to produce large  $Q_4$  subpopulations (Figure 6). At larger electric field strengths and durations, this  $Q_3$  subpopulation ultimately blends into the rest as Pro enters the cells more rapidly ( $Q_4$  subpopulation).<sup>20,21</sup>

For PEF applications with pulse durations of nanoseconds to tens of microseconds, it has been shown that cells exhibit increasing delays of  $\geq 5$  minutes between application and a rapid influx of Pro.<sup>21,38,47</sup> In the present case, this transition would fall into the  $Q_3$  subpopulation, which was observed to increase in cells exposed to applications of 100 to 1000 microseconds at 170 to 400 kV/m (Figure 7). However, this lower strength–duration threshold still allows for the uptake of 25% of the external concentration of Pro (Figure 5). While our data indicate that as many as 40% of a population of cells exposed to a single pulse are in the  $Q_3$  subpopulation, others have suggested that this fraction could be as high as 83% for nanosecond pulses delivered in rapid succession.<sup>47</sup> These schemes induce delays on the order of 1000 seconds prior to appreciable membrane permeabilization. It was also observed that the fraction of cells in this state decreased when the time period over which the application was delivered increased.<sup>47</sup> These data are consistent with our results and implicate a transitional region in the

electric field strength–pulse duration space ( $Q_3$ ) that emerges for parameters that are insufficient to outright cause immediate permeabilization. During our study, PBS, SFDF, and HEPES buffers were used to provide a more thorough investigation into post-PEF cell behaviors. Interestingly, cells immersed in the HEPES buffer appear to exhibit a homogenous response, compared to cells treated in PBS or SFDF. While similar trends exist in the appearance and disappearance of the  $Q_3$  subpopulation with increasing PEF strengths and durations for each medium, the  $Q_4$  subpopulation begins to contain the majority cells at lower strengths and durations for the cells treated in the HEPES buffer (Figure 7). One explanation could be that the increased permittivity due to zwitterions<sup>60,61</sup> and the decreased conductivity due to the sucrose<sup>45,62</sup> in the HEPES buffer increases the electrical relaxation time of the membrane. In this way, effects of small variations in the capacitance of individual cell membranes could be reduced and therefore effectively reduce the variation in cellular response to PEFs. The increased permittivity of the HEPES buffer could also enhance the electrical force on the cell membrane and lower the strength–duration threshold at which appreciable EP is observed.<sup>60,62</sup> This delay is present in cells treated in each buffer and therefore may be the result of an osmotic pressure difference. Cells that experience a prolonged permeabilization may be more efficiently killed by an increased osmotic pressure difference change postpulse, thereby minimizing thermal damage and improving tumor ablation protocols.<sup>63</sup> Regardless of the mechanism, cells belonging to the  $Q_3$  subpopulation exhibit a prolonged Pro uptake and ultimately yield significant intracellular Pro concentrations ( $[Pro]_f \geq [Pro]^{ext}/4$ ; Figure 6). If such a mechanism could be exploited to affect cells *in vivo*, EP-based applications and therapies could involve lower electric field strengths, resulting in significantly less thermal damage than present application paradigms.

Several complexities are inherent in the data we present here. First, during the chemical permeabilization, the Triton X-100 concentration was above the critical micelle concentration, which could influence the effective concentration of Pro in the extracellular buffer during the calibration experiments. We do not anticipate this affecting our permeability measurements as the correlation between fluorescence intensity and Pro concentration is linear (Supplemental Figure 3) and appears in both the numerator and denominator of Equation 1. However, the Pro uptake measurements may be overestimates in the presence of micelles–Pro interactions in the calibration buffer.

Second, the ringing on the rising and falling edges of the pulses we use in our experiments could complicate the interpretation of the cellular response to PEF applications. However, our data for 1-microsecond pulse applications differ little from the untreated controls, indicating minimal permeabilization of the cell membrane (Figure 3), while similar peak electric field strengths are achieved during the rising and falling edges of longer duration waveform. The difference between these waveforms is consequently the duration between the ringing on the rising edge and the falling edge, and therefore we expect this component of the waveform to dominate the

cellular EP response. For this reason, we do not anticipate these oscillations to have a significant impact on the membrane permeabilization following a single pulse and consider further analysis of the effects of these waveforms to be outside the scope of the present study.

## Conclusion

We report a research method for quantitatively determining a membrane's diffusive permeability to Pro using fluorescence microscopy. We determine the diffusive permeability to Pro for pulse durations of 1 to 1000 microseconds and electric field strengths of 170 to 400 kV/m in 3 buffers and find that the cell membrane permeability to Pro ions can reach  $1.3 \pm 0.4 \times 10^{-8}$  m/s. We also show that the increased permeability persists for at least 30 minutes. Further, for Pro, the initial influx rate is a strong predictor of a cell's final intracellular Pro concentration. Finally, we identify a subpopulation of cells that have larger concentrations of Pro after a prolonged uptake (100 seconds) than cells exposed to smaller fields. Our results both technically enable and experimentally provide a basis for future quantitative investigations that (1) determine lethal permeabilities, (2) examine transitions in Pro uptake kinetics, and (3) provide experimental uptake rates for comparison with predictions of cell-level computational models.

## Acknowledgments

The authors would like to acknowledge the ICTAS Center for Engineered Health for their gracious financial support of this work.


## Declaration of Conflicting Interests

The author(s) declared the following potential conflicts of interest with respect to the research, authorship, and/or publication of this article: D. C. Sweeney, J. C. Weaver, and R. V. Davalos have filed a patent application related to this work.

## Funding

The author(s) disclosed receipt of the following financial support for the research, authorship, and/or publication of this article: Funding for this work was graciously provided for DCS and RVD by the NSF CAREER Award CBET-1055913, the NSF IGERT DGE-09661, and the NIH P01-CA207206. Funding for JCW was graciously provided by AFOSR MURI Grant FA9550-15-1-0517.

## ORCID iD

Daniel C. Sweeney  <http://orcid.org/0000-0002-1289-1627>

## Supplemental Material

Supplemental material for this article is available online.

## References

- Rols MP, Teissié J. Electroporation of mammalian cells: quantitative analysis of the phenomenon. *Biophys J*. 1990;58(5):1089-1098.
- Sixou S, Teissié J. Exogenous uptake and release of molecules by electroloaded cells: a digitized videomicroscopy. *Bioelectrochem Bioenerg*. 1993;31(3):237-257.
- Davalos RV, Mir LM, Rubinsky B. Tissue ablation with irreversible electroporation. *Ann Biomed Eng*. 2005;33(2):223-231.
- Rems L, Miklavčič D. Tutorial: electroporation of cells in complex materials and tissue. *J Appl Phys*. 2016;119(20):201101.
- Yang Y, Moser MAJ, Zhang E, Zhang W, Zhang B. Development of a statistical model for cervical cancer cell death with irreversible electroporation in vitro. *PLoS One*. 2018;13(4):e0195561.
- Piñero J, López-Baena M, Ortiz T, Cortés F. Apoptotic and necrotic cell death are both induced by electroporation in HL60 human promyeloid leukaemia cells. *Apoptosis*. 1997;2(3):330-336.
- Goswami I, Coutermarsh-Ott S, Morrison RG, et al. Irreversible electroporation inhibits pro-cancer inflammatory signaling in triple negative breast cancer cells. *Bioelectrochemistry*. 2017;13:42-50.
- Ryttsén F, Farre C, Brennan C, et al. Characterization of single-cell electroporation by using patch-clamp and fluorescence microscopy. *Biophys J*. 2000;79(4):1993-2001.
- Rols MP, Teissié J. Electroporation of mammalian cells to macromolecules: control by pulse duration. *Biophys J*. 1998;75(3):1415-1423.
- Canatella PJ, Karr JF, Petros JA, Prausnitz MR. Quantitative study of electroporation-mediated molecular uptake and cell viability. *Biophys J*. 2001;80(2):755-764.
- Tieleman DP, Marrink SJ, Berendsen HJC. A computer perspective of membranes: molecular dynamics studies of lipid bilayer systems. *Biochim Biophys Acta*. 1997;1331(3):235-270.
- Tarek M. Membrane electroporation: a molecular dynamics simulation. *Biophys J*. 2005;88(6):4045-4053.
- Son RS, Smith KC, Gowrishankar TR, Vernier PT, Weaver JC. Basic features of a cell electroporation model: illustrative behavior for two very different pulses. *J Membr Biol*. 2014;247(12):1209-1228.
- Vernier PT, Ziegler MJ, Sun Y, Chang WV, Gundersen MA, Tieleman DP. Nanopore formation and phosphatidylserine externalization in a phospholipid bilayer at high transmembrane potential. *J Am Chem Soc*. 2006;128(19):6288-6289.
- Kinosita KJ, Tsong TY. Formation and resealing of pores of controlled sizes in human erythrocyte membrane. *Nature*. 1977;268(4):438-441.
- Kotnik T, Maček-Lebar A, Miklavčič D, Mir LM. Evaluation of cell membrane electroporation by means of a nonpermeant cytotoxic agent. *Biotechniques*. 2000;28(5):921-926.
- Lebar AM, Miklavčič D. Cell electroporation to small molecules in vitro: control by pulse parameters. *Radiol Oncol*. 2001;35(3):193-202.
- Bowman AM, Nesin OM, Pakhomova ON, Pakhomov AG. Analysis of plasma membrane integrity by fluorescent detection of TI(+) uptake. *J Membr Biol*. 2010;236(1):15-26.
- Shirakashi R, Sukhorukov VL, Tanasawa I, Zimmermann U. Measurement of the permeability and resealing time constant of the electroporated mammalian cell membranes. *Int J Heat Mass Transf*. 2004;47(21):4517-4524.

20. Kennedy SM, Aiken EJ, Beres KA, et al. Cationic peptide exposure enhances pulsed-electric-field-mediated membrane disruption. *Plos One*. 2014;9(3):e92528.
21. Kennedy SM, Ji Z, Hedstrom JC, Booske JH, Hagness SC. Quantification of electroporative uptake kinetics and electric field heterogeneity effects in cells. *Biophys J*. 2008;94(12):5018-5027.
22. Sadik MM, Li J, Shan JW, Shreiber DI, Lin H. Quantification of propidium iodide delivery using millisecond electric pulses: experiments. *Biochim Biophys Acta*. 2013;1828(4):1322-1328.
23. Sweeney DC, Reberšek M, Dermol J, Rems L, Miklavčič D, Davalos RV. Quantification of cell membrane permeability induced by monopolar and high frequency bipolar bursts of electrical pulses. *Biochim Biophys Acta*. 2016;1858(11):2689-2698.
24. Bonakdar M, Wasson EM, Lee YW, Davalos RV. Electroporation of brain endothelial cells on chip toward permeabilizing the blood-brain barrier. *Biophys J*. 2016;110(2):503-513.
25. Geuzaine C. Gmsh: a three-dimensional finite element mesh generator with built-in pre- and post-processing facilities. *Int J Numer Methods Eng*. 2009;79(11):1309-1331.
26. Logg A, Mardal KA, Wells G. *Automated Solution of Differential Equations by the Finite Element Method: The FEniCS Book*. Heidelberg, Germany: Springer-Verlag Berlin Heidelberg; 2012:84.
27. Kotnik T, Pucihar G, Reberšek M, Miklavčič D, Mir LM. Role of pulse shape in cell membrane electroporation. *Biochim Biophys Acta*. 2003;1614(2):193-200.
28. Satkauskas S, Bureau MF, Puc M, et al. Mechanisms of in vivo DNA electrotransfer: respective contributions of cell electroporation and DNA electrophoresis. *Mol Ther*. 2002;5(2):133-140.
29. Schindelin J, Arganda-carreras I, Frise E, et al. Fiji – an open source platform for biological image analysis. *Nat Methods*. 2012;9(7):676.
30. Carpenter AE, Jones TR, Lamprecht MR, et al. CellProfiler: image analysis software for identifying and quantifying cell phenotypes. *Genome Biol*. 2006;7(10):R100.
31. Fedorov A, Beichel R, Kalpathy-Cramer J, et al. 3D slicer as an image computing platform for the quantitative imaging network. *Magn Reson Imaging*. 2012;30(9):1323-1341.
32. Cignoni P, Callieri M, Corsini M, Dellepiane M, Ganovelli F, Ranzuglia G. MeshLab: an open-source mesh processing tool. In: *Sixth Eurographics Italian Chapter Convergence*. Eurographics Italian chapter conference; 2008:129-136.
33. Seksek O, Biwersi J, Verkman AS. Translational diffusion of macromolecule-sized solutes in cytoplasm and nucleus. *J Cell Biol*. 1997;138(1):131-142.
34. Neumann E, Toensing K, Kakorin S, Budde P, Frey J. Mechanism of electroporative dye uptake by mouse B cells. *Biophys J*. 1998;74(1):98-108.
35. Pucihar G, Kotnik T, Miklavcic D, Teissié J. Kinetics of transmembrane transport of small molecules into electroporated cells. *Biophys J*. 2008;95(6):2837-2848.
36. Lukacs GL, Haggie P, Seksek O, Lechardeur D, Freedman N, Verkman AS. Size-dependent DNA mobility in cytoplasm and nucleus. *J Biol Chem*. 2000;275(3):1625-1629.
37. Verkman AS. Solute and macromolecule diffusion in cellular aqueous compartments. *Trends Biochem Sci*. 2002;27(1):27-33.
38. Deng J, Schoenbach KH, Buescher ES, Hair PS, Fox PM, Beebe SJ. The effects of intense submicrosecond electrical pulses on cells. *Biophys J*. 2003;84(4):2709-2714.
39. Verkman AS. Membrane biology water permeability measurement in living cells and complex tissues. *J Membr Biol*. 2000;173(2):73-87.
40. Zarnitsyn V, Rostad CA, Prausnitz MR. Modeling transmembrane transport through cell membrane wounds created by acoustic cavitation. *Biophys J*. 2008;95(9):4124-4138.
41. Kao HP, Abney JR. Determinants of the translational mobility of a small solute in cell cytoplasm. *J Cell Biol*. 1993;120(1):175-184.
42. Bicknese S, Periasamy N, Shohet SB, Verkman AS. Cytoplasmic viscosity near the cell plasma membrane: measurement by evanescent field frequency-domain microfluorimetry. *Biophys J*. 1993;65(3):1272-1282.
43. Lebar AM, Kopitar NA, Ihan K, Sersa G, Miklavcic D. Significance of treatment energy in cell electroporation. *Electro Magnetobiol*. 1998;17(2):255-262.
44. Pucihar G, Krmelj J, Reberšek M, Napotnik TB, Miklavčič D. Equivalent pulse parameters for electroporation. *IEEE Trans Biomed Eng*. 2011;58(11):3279-3288.
45. Silve A, Leray I, Poignard C, Mir LM. Impact of external medium conductivity on cell membrane electroporation by microsecond and nanosecond electric pulses. *Sci Rep*. 2016;6:19957.
46. Neumann E. Membrane electroporation and direct gene transfer. *J Electroanal Chem*. 1992;343(1-2):247-267.
47. Pakhomova ON, Gregory BW, Khorokhorina VA, Bowman AM, Xiao S, Pakhomov AG. Electroporation-induced electrosensitization. *PLoS One*. 2011;6(2):36-38.
48. Huang Y, Rubinsky B. Micro-electroporation: improving the efficiency and understanding of electrical permeabilization of cells. *Biomed Microdevices*. 1990;2(2):145-150.
49. Frandsen SK, Gissel H, Hojman P, Tramm T, Eriksen J, Gehl J. Direct therapeutic applications of calcium electroporation to effectively induce tumor necrosis. *Cancer Res*. 2012;72(6):1336-1341.
50. Frandsen SK, Gissel H, Hojman P, Eriksen J, Gehl J. Calcium electroporation in three cell lines: a comparison of bleomycin and calcium, calcium compounds, and pulsing conditions. *Biochim Biophys Acta*. 2014;1840(3):1204-1208.
51. Hansen EL, Sozer EB, Romeo S, Frandsen SK, Vernier PT, Gehl J. Dose-dependent ATP depletion and cancer cell death following calcium electroporation, relative effect of calcium concentration and electric field strength. *PLoS One*. 2015;10(4):1-12.
52. Tolstykh GP, Thompson GL, Beier HT, Steelman ZA, Ibay BL. nsPEF-induced PIP2 depletion, PLC activity and actin cytoskeletal cortex remodeling are responsible for post-exposure cellular swelling and blebbing. *Biochem Biophys Rep*. 2016;9:36-41.
53. Whetton AD, Dexter TM. Effect of haematopoietic cell growth factor on intracellular ATP levels. *Nature*. 1983;303(5918):629-631.
54. Calderwood SK, Bump EA, Stevenson MA, Van Kersen I, Hahn GM. Investigation of adenylate energy charge, phosphorylation

- potential, and ATP concentration in cells stressed with starvation and heat. *J Cell Physiol.* 1985;124(2):261-268.
55. Fine EJ, Miller A, Quadros EV, Sequeira JM, Feinman RD. Acetate reduces growth and ATP concentration in cancer cell lines which over-express uncoupling protein 2. *Cancer Cell Int.* 2009;9:14.
56. Rols MP, Delteil C, Muriel G, Teissie J. Control by ATP and ADP of voltage-induced mammalian-cell-membrane permeabilization, gene transfer and resulting expression. *Eur J Biochem.* 1998; 254(2):382-388.
57. Smith KC. *A Unified Model of Electroporation and Molecular Transport.* Cambridge, MA: Massachusetts Institute of Technology; 2011.
58. Poellmann MJ, Lee RC. Repair and regeneration of the wounded cell membrane. *Regen Eng Transl Med.* 2017;3(3):111-132.
59. Lee RC, Zhang D, Hannig J. Biophysical injury mechanisms in electrical shock trauma. *Annu Rev Biomed.* 2000;2(1): 477-509.
60. Arnold WM, Zimmermann U. Dielectric properties of zwitterion solutions. *Biochem Soc Trans.* 1993;21(4):475S.
61. Gagnon Z, Chang HC. Aligning fast alternating current electroosmotic flow fields and characteristic frequencies with dielectrophoretic traps to achieve rapid bacteria detection. *Electrophoresis.* 2005;26(19):3725-3737.
62. Malmberg CG, Maryott AA. Dielectric constants of aqueous solutions of dextrose and sucrose. *J Res Natl Bur Stand (1934).* 1950; 45(4):299.
63. Weaver JC, Son RS, Gowrishankar TR, Sweeney DC, Davalos RV. Methods for inducing electroporation and tissue ablation. *US Patent App.* 2016;15(179):310.